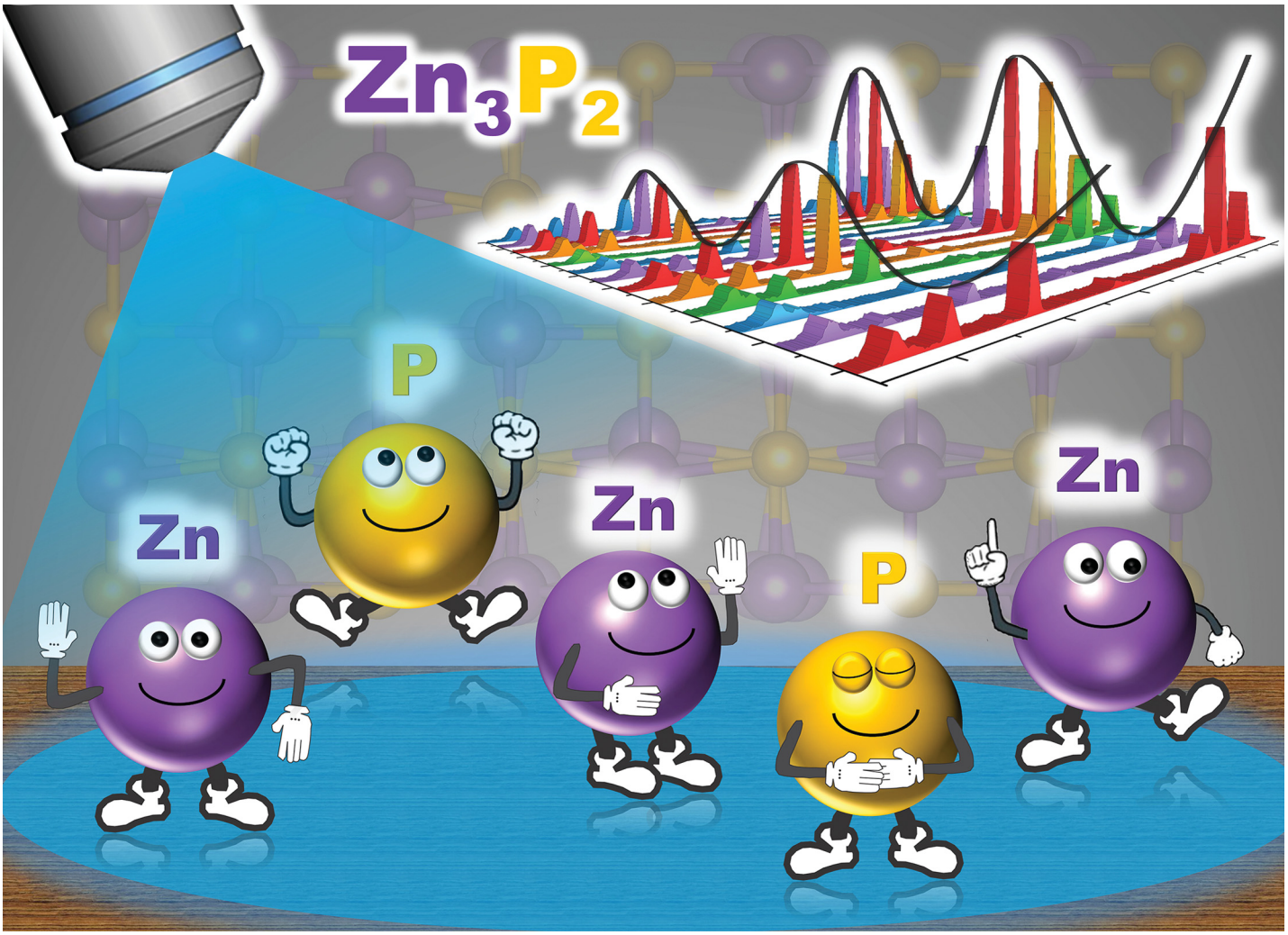

Showcasing research from the Laboratory of Semiconductor Materials (LMSC) at École Polytechnique Fédérale de Lausanne (EPFL), Switzerland

Raman tensor of zinc-phosphide (Zn_3P_2): from polarization measurements to simulation of Raman spectra

LMSC is investigating structural and functional properties of new earth-abundant semiconductor materials, such as zinc phosphide (Zn_3P_2), for next generation photovoltaic applications. In this work, we combine angle-resolved polarization Raman measurements and density functional theory calculations to determine the Raman tensor of Zn_3P_2. These results provide a stepping stone to using Raman spectroscopy for identification and characterization of defects, a key feature for further optimization of this material for high efficiency solar cell devices.

As featured in:

See Mirjana Dimitrievska *et al.*, *Phys. Chem. Chem. Phys.*, 2022, **24**, 63.

ROYAL SOCIETY OF CHEMISTRY

rsc.li/pccp

Registered charity number: 207890

PCCP

ROYAL SOCIETY OF CHEMISTRY

PAPER

View Article Online
View Journal | View Issue

Cite this: *Phys. Chem. Chem. Phys.*, 2022, **24**, 63

Raman tensor of zinc-phosphide (Zn_3P_2): from polarization measurements to simulation of Raman spectra†

Mischa Flór,[a] Elias Z. Stutz,[a] Santhanu P. Ramanandan,[a] Mahdi Zamani,[a] Rajrupa Paul,[a] Jean-Baptiste Leran,[a] Alexander P. Litvinchuk,[b] Anna Fontcuberta i Morral[ac] and Mirjana Dimitrievska*[a]

Zinc phosphide (Zn_3P_2) is a II–V compound semiconductor with promising photovoltaic and thermoelectric applications. Its complex structure is susceptible to facile defect formation, which plays a key role in further optimization of the material. Raman spectroscopy can be effectively used for defect characterization. However, the Raman tensor of Zn_3P_2, which determines the intensity of Raman peaks and anisotropy of inelastic light scattering, is still unknown. In this paper, we use angle-resolved polarization Raman measurements on stoichiometric monocrystalline Zn_3P_2 thin films to obtain the Raman tensor of Zn_3P_2. This has allowed determination of the Raman tensor elements characteristic for the A_{1g}, B_{1g} and B_{2g} vibrational modes. These results have been compared with the theoretically obtained Raman tensor elements and simulated Raman spectra from the lattice-dynamics calculations using first-principles force constants. Excellent agreement is found between the experimental and simulated Raman spectra of Zn_3P_2 for various polarization configurations, providing a platform for future characterization of the defects in this material.

Received 21st September 2021,
Accepted 23rd November 2021

DOI: 10.1039/d1cp04322f

rsc.li/pccp

1 Introduction

Zinc Phosphide (Zn_3P_2) is a semiconductor made of earth-abundant elements, with promising properties for photovoltaic and thermoelectric applications.[1–14] Recently, Zn_3P_2 has also been receiving more attention due to its facile synthesis into nanostructures,[15–18] as well as breakthroughs in growth quality.[19–21] One attractive feature of Zn_3P_2 is a large and complex tetragonally distorted fluorite lattice, which ensures phase stability over a substantial range of compositions, thanks to the disseminated vacancies.[22,23] This offers tunability for defect engineering and doping, a stepping stone to achieving efficient Zn_3P_2-based devices.[24–26] An important element to advancing the defect engineering in Zn_3P_2 and related compounds, is developing a fast and non-destructive method for defect characterization and quantification. [25,26]

Raman spectroscopy is a versatile tool for studying structural changes in materials, as it provides information about the vibrational properties of the material both due to the crystal structure and chemical composition. Considering that phonons represent collective vibrational oscillations of atoms inside the lattice, any kind of structural irregularities, such as defects or impurities, will strongly affect them. Thus, Raman spectroscopy may serve as a powerful technique for providing information on phase,[27] defects,[28–31] inhomogeneities,[32] and crystallinity.[33]

In order to successfully use Raman spectroscopy for identification of defects, it is necessary to build methodologies which combine both experimental and computational tools. A common challenge in experimental studies is distinguishing the exact type and quantity of defects present. This leads to difficulties in establishing correlation between certain types of defects and changes in the Raman features. Computational tools could help in this case, by simulating Raman spectra of materials with various types and concentrations of defects. However, these simulations are usually challenging, as they require building very large supercells, which result in high computational costs. Recently, a new method for simulating Raman spectra of defective materials with a small computational cost was proposed by Hashemi *et al.*[34] These simulations use vibrational eigenvectors of the defective system and the Raman tensors of the pristine system to calculate the Raman spectra of a defective material. Therefore, the first step towards application of Raman

[a] *Laboratory of Semiconductor Materials, Institute of Materials, Faculty of Engineering, Ecole Polytechnique Fédérale de Lausanne, 1015 Lausanne, Switzerland. E-mail: mirjana.dimitrievska@epfl.ch*
[b] *Texas Center for Superconductivity and Department of Physics, University of Houston, Houston, Texas 77204-5002, USA*
[c] *Institute of Physics, Faculty of Basic Sciences, Ecole Polytechnique Fédérale de Lausanne, 1015 Lausanne, Switzerland*

† Electronic supplementary information (ESI) available. See DOI: 10.1039/d1cp04322f

spectroscopy for defect identification in Zn_3P_2 is reliable determination of its Raman tensor elements on the reference samples.

Previous work on Raman characterization of Zn_3P_2 was mostly aimed at providing reference Raman spectra. First elucidations on the properties of Raman modes were proposed from group theory analysis,[22] following by experimental investigations,[23,35] and more recently from first principle calculations based on density functional theory (DFT).[35] Stutz *et al.*[35] have used DFT calculations and Raman polarization measurements on a single crystal Zn_3P_2 nanowires, allowing identification of 33 phonon modes which were attributed to their respective symmetries. To the best of our knowledge, Raman tensor elements of Zn_3P_2 have not yet been investigated or reported, even though they are essential for establishing tangible correlations between Raman mode intensities and the existence of defects.[36] Additionally, Raman spectra simulations of Zn_3P_2 have been challenging to perform due to the large number of atoms involved in the Zn_3P_2 crystal lattice.

In this work, we provide new insights on the vibrational properties of stoichiometric monocrystalline Zn_3P_2 thin films using angle-resolved polarization Raman measurements and first-principle calculations. Particular focus is put on the intensity evolution of the Raman modes under different polarization configurations. This has allowed determination of the Raman tensor elements characteristic for the A_{1g}, B_{1g} and B_{2g} vibrational modes. These results have been compared with the theoretically obtained Raman tensor elements and simulated Raman spectra from the lattice-dynamics calculations.

2 Experimental methods

Sample preparation

Monocrystalline Zn_3P_2 thin films were grown by molecular-beam epitaxy on InP(100) substrates. The growth methods are extensively explained in reference[19].

Polarized Raman spectroscopy

Polarized Raman spectroscopy was realized in the backscattering configuration at 12 K. The 488 nm line of a Coherent sapphire

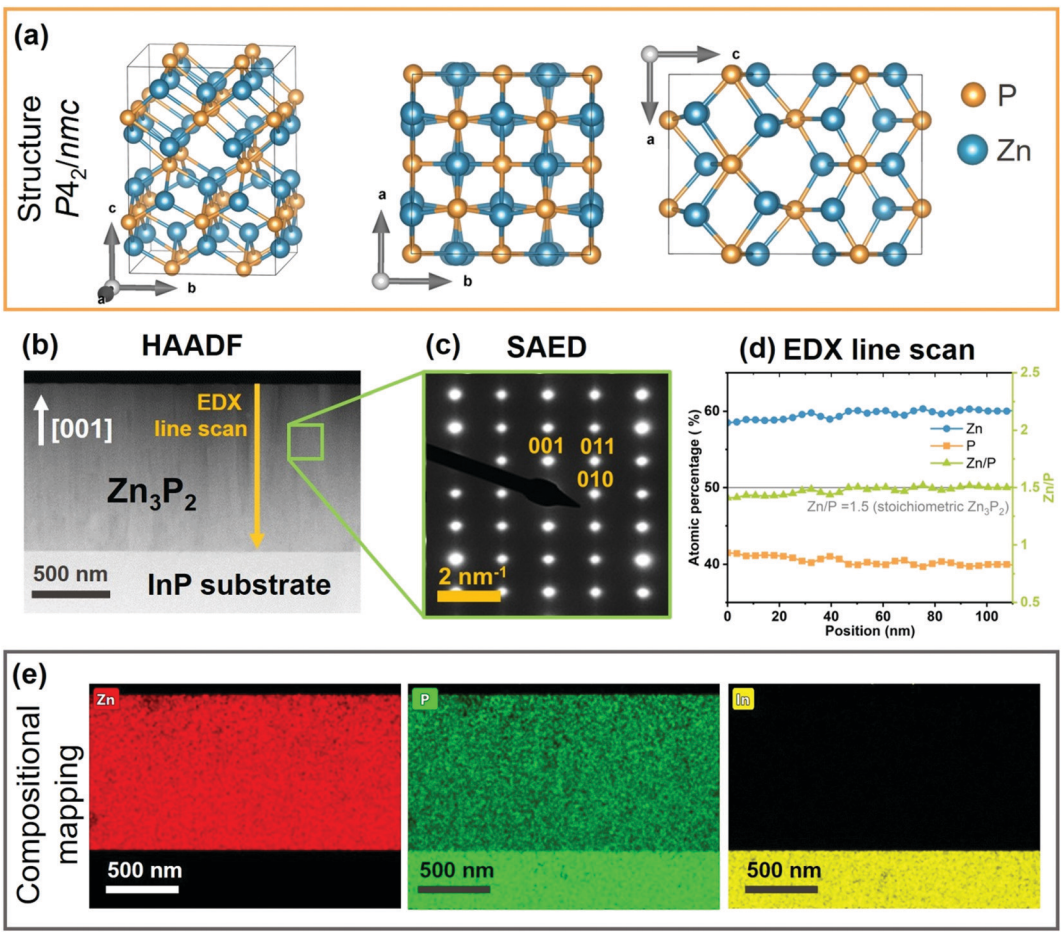

Fig. 1 Structural and compositional characterization of Zn_3P_2 thin film: (a) Crystal structure representation of tetragonal Zn_3P_2 unit cell along different crystal planes. (b) HAADF image of the Zn_3P_2 thin film cross section along with (c) the SAED pattern confirming its monocrystalline nature. The patterns are indexed with respect to the tetragonal ($P4_2/nmc$) unit cell. (d) EDX line scan and (e) compositional mapping of the Zn_3P_2 thin film showing uniform distribution of Zn and P along the cross section, without any In intermixing from the InP(100) substrate. The measured composition of the Zn_3P_2 thin film is Zn/P = 1.51 ± 0.02.

optically pumped semiconductor laser was used for excitation. The beam was focused on the sample with a microscope objective with a numerical aperture of 0.75, resulting in a 1 μm diameter spot, reaching a radiant power of the order of 700 μW. The incident flux was controlled combining a half-waveplate and a polarization beam-splitter. The incident polarization was controlled with a subsequent half-waveplate. The backscattered light goes through a linear polarizer, and a last half-waveplate directs the polarization parallel to the entrance slit of a TriVista triple spectrometer with 900, 900 and 1800 cm^{-1} gratings in subtractive mode and a Princeton Instrument liquid nitrogen cooled multichannel CCD PyLoN camera. The polarization direction is described with respect to a reference direction on the setup and moves in the *xy* crystallographic plane of the sample. All the spectra were calibrated based on the reference sulfur Raman spectrum.

Structural and compositional characterization

High angle annular dark field (HAADF) STEM image and energy dispersive X-ray spectroscopy (EDS) elemental maps were collected using FEI Talos transmission electron microscope operating at 200 kV.

Density functional theory calculations

The first-principles calculations of the electronic ground state of the tetragonally structured Zn_3P_2 were performed within the local density approximation using Ceperly–Adler functional,[37,38] as implemented in the CASTEP code.[39] Norm-conserving pseudopotentials were used. The cutoff energy for the plane wave basis was set to 600 eV. A selfconsistent-field (SCF) tolerance better than 10^{-7} eV per atom and the phonon SCF threshold of 10^{-12} eV per atom were imposed. Prior to performing calculations, the structure was relaxed so that forces on atoms in the equilibrium position did not exceed 2 meV $Å^{-1}$ and the residual stress was below 5 MPa. Experimentally determined lattice parameters from ref. 40 were used as a starting point. An integration over the Brillouin zone was performed over a 3 × 3 × 2 Monkhorst–Pack grid in reciprocal space.

3 Results and discussion

3.1 Structural and compositional characterization of Zn_3P_2 thin film

We start by providing evidence of the crystal structure and composition of the sample investigated here. Fig. 1(a) presents the crystal structure of Zn_3P_2 by visualizing it from three different zone axes. The lattice has a tetragonal symmetry with $P4_2/nmc$ (D_{4h}^{15}) space group. The unit cell contains 8 formula units ($Zn_{24}P_{16}$) with 40 atoms total, and lattice parameters of a = 8.0785 Å and c = 11.3966 Å.[40] Cations (Zn) and anions (P) are stacked in alternate planes along the *c*-axis. The unit cell can be described as an assembly of four cubic sub-cells similar to the fluoride structure, except for one quarter of the cations missing. These are Zn vacancies located on the body diagonals of the cubes. The irregular ordering of these vacancies results in distortions that lowers the symmetry, which explains the four times larger volume compared to fluoride-like unit cells. Zn cations form distorted tetrahedrons of which the vertices are the P anions. The P anions are surrounded by 8 voids of which 6 are occupied by the Zn cations.

Fig. 1(b) dispatches the cross sectional HAADF image of the synthesized Zn_3P_2 thin film on InP(100) substrate. Selective area electron diffraction (SAED) pattern (Fig. 1(c)) measured on the Zn_3P_2 layer confirms the monocrystalline nature of the sample. Calculations of atomic distances based on the SAED pattern corroborate the formation of the tetragonal ($P4_2/nmc$) unit cell of Zn_3P_2 and the growth direction along the *c* crystal axis ([001]), which is perpendicular to the substrate. The compositional assessment, performed by STEM-EDX (Fig. 1(d)), indicates formation of close to stochiometric phase with Zn/P = 1.51 ± 0.02 (compared to stochiometric Zn/P = 1.5). Further, a homogenous distribution of Zn and P with no detectable phase segregation or intermixing with indium (In) is observed from the compositional maps shown in Fig. 1(e). This is within the spatial and chemical composition resolution of our experiments and agrees well with previous studies.[19]

3.2 Raman tensors of Zn_3P_2

Group theory analysis predicts 39 Raman active modes for Zn_3P_2 structure with the following irreducible representations:[41]

$$\Gamma_{\text{Raman}} = 9A_{1g} + 10B_{1g} + 4B_{2g} + 16E_g \quad (1)$$

where the A and B modes correspond to non-degenerate modes, while the E modes are doubly degenerate.

Under non-resonant conditions, the Raman tensors for the Raman-active phonon modes are defined as:

$$\Re(A_{1g}) = \begin{pmatrix} a & 0 & 0 \\ 0 & a & 0 \\ 0 & 0 & b \end{pmatrix} \quad \Re(B_{1g}) = \begin{pmatrix} c & 0 & 0 \\ 0 & -c & 0 \\ 0 & 0 & 0 \end{pmatrix} \quad \Re(B_{2g}) = \begin{pmatrix} 0 & d & 0 \\ d & 0 & 0 \\ 0 & 0 & 0 \end{pmatrix} \quad \Re(E_g) = \begin{pmatrix} 0 & 0 & e \\ 0 & 0 & e \\ e & e & 0 \end{pmatrix} \quad (2)$$

where a, b, c, d and e are the Raman tensor coefficients (elements).

The scattering intensity of each mode in the Raman spectra is defined by:[42]

$$I_S \propto C(\omega_p)\left|\vec{e_i}\cdot\Re\cdot\vec{e_S}\right|^2. \quad (3)$$

where $\vec{e_i}$ and $\vec{e_S}$ are the unitary polarization vectors of the incident light and backscattered light, respectively. The coefficient $C(\omega_p)$, while usually omitted in the literature, should be considered here, as it describes the dependence of the Raman mode intensity from the phonon frequency ω_p and the incident laser frequency ω_i. It is defined as:[42]

$$C(\omega_p) = \frac{\omega_i(\omega_i-\omega_p)^3}{\omega_p\left[1-\exp(-\hbar\omega_p/k_BT)\right]}. \quad (4)$$

where $\hbar = h/2\pi$, with h being the Planck constant, k_B is the Boltzmann constant and T is the temperature of the measurements.

Considering the configuration of the Raman measurements as shown in Fig. 2, the incident $\vec{e_i}$ and backscattering $\vec{e_S}$ polarization unit vectors can be defined as:

$$\vec{e_i} = (\sin\theta \quad \cos\theta \quad 0), \quad (5)$$

$$\vec{e_S}^{\parallel} = \begin{pmatrix}\sin\theta\\ \cos\theta\\ 0\end{pmatrix} \text{ and } \vec{e_S}^{\perp} = \begin{pmatrix}\cos\theta\\ -\sin\theta\\ 0\end{pmatrix} \quad (6)$$

where θ is the polarization angle with respect to the [010] axis, while the signs $\parallel$ and $\perp$ correspond to either parallel or perpendicular polarization, respectively.

Combination of eqn (3)–(6) yields the Raman intensity dependency from the polarization angle for different phonon modes, which are presented in Table 1. We find that changes in the polarization angle lead to selective activation or cancelling of phonon modes. In the case where polarization Raman measurements are performed incident onto the (001) basal plane (Fig. 2), the E_g modes are silent while the other modes vary according to the polarization configuration. The intensity of the B_{1g} and B_{2g} modes should periodically change in phase opposition of $\pi/4$ (45°), while the intensity of the A_{1g} mode is constant in parallel configuration and cancelled in perpendicular.

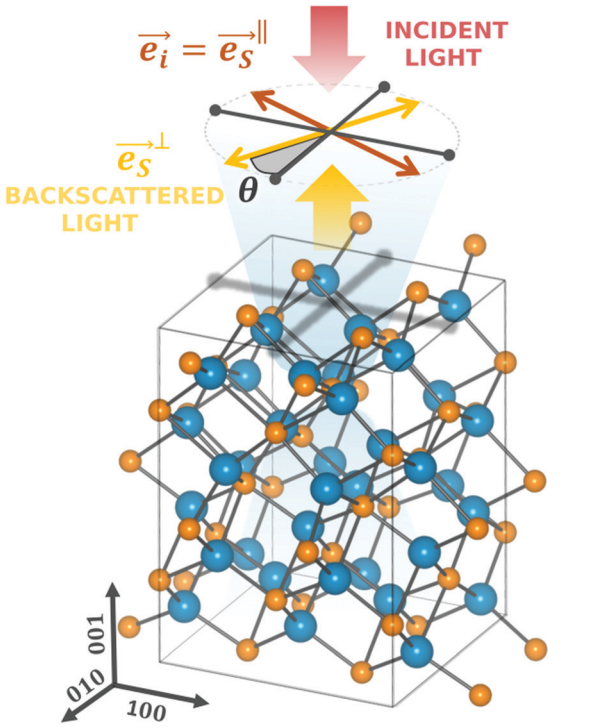

Fig. 2 Schematic of the Raman scattering polarization measurements. Raman measurements are performed on (001) basal plane with incident laser light (wide red arrow) projected along the z-axis ([001] direction). The incident light polarization and the output polarization in perpendicular configuration are represented by the thin red and yellow arrows, respectively. The black arrows indicate the x and y axis of the crystal corresponding to [100] and [010] directions, respectively.

Table 1 Angular dependencies of Raman modes intensity for tetragonal Zn_3P_2, in parallel and perpendicular measurement configurations on (001) basal plane, with θ being the polarization angle between $\vec{e_i}$ and (010)

	Parallel configuration	Perpendicular configuration
A_{1g} phonon modes	$C(\omega_p)\cdot a^2$	0
B_{1g} phonon modes	$C(\omega_p)\cdot\lvert c\cdot\cos 2\theta\rvert^2$	$C(\omega_p)\cdot\lvert c\cdot\sin 2\theta\rvert^2$
B_{2g} phonon modes	$C(\omega_p)\cdot\lvert d\cdot\sin 2\theta\rvert^2$	$C(\omega_p)\cdot\lvert d\cdot\cos 2\theta\rvert^2$
E_g phonon modes	0	0

3.3 Angle-resolved Raman polarization measurements of Zn_3P_2

We move now to the experimental Raman spectroscopy measurements. Fig. 3 presents the polarization Raman spectra performed on monocrystalline Zn_3P_2 thin film, in parallel and perpendicular configurations for various polarization angles (θ) in the range from 0 to 180°. All spectra were acquired at low temperature (12 K) to reduce thermal effects on the Raman peaks, leading to increased intensity and reduced peak-broadening due to increased phonon lifetime at lower temperatures. We chose 488 nm laser to avoid resonance Raman effects, as based on the band structure calculations for Zn_3P_2,[14] there are no electronic bands in the energy region corresponding to the laser excitation. Detailed analysis of the complete set of Raman spectra allowed resolution of 17 peaks which intensity evolves according to the expected behavior in Table 1, enabling attribution of each peak to A_{1g}, B_{1g} or B_{2g} mode as further elucidated in the next paragraphs.

We highlight four representative Raman peaks centered at 148, 224, 287 and 341 cm^{-1} with characteristic polarization intensity behavior in Fig. 3. Clearly, the intensity of the highlighted peaks varies with θ for peaks at 148 and 341 cm^{-1}, while these changes are less obvious for peaks at 224 and 287 cm^{-1}. This behavior can be visualized in a more accurate manner by plotting the intensity as a function of θ as in Fig. 4(a). Fig. 4(a) illustrates very clearly which peaks exhibit either a periodic change with θ or no variation at all. Fig. 4(b–e) plot the intensity values with respect to θ, allowing for a fit of the curves. Based on the fittings, it is possible to unambiguously identify the symmetry type of each peak observed in the Raman spectra of Zn_3P_2. Raman

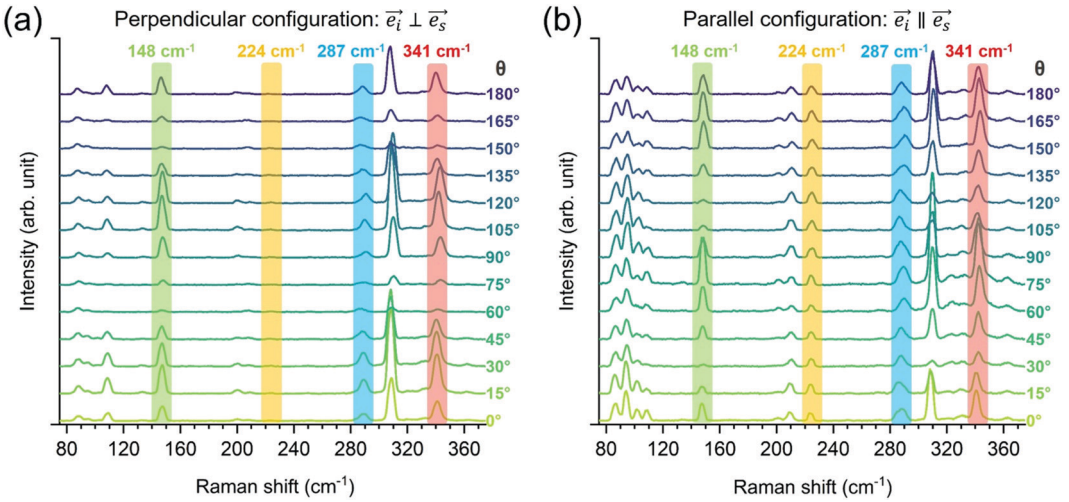

Fig. 3 Polarization Raman spectra of monocrystalline Zn_3P_2 thin film measured for various polarization angles (θ) in (a) perpendicular and (b) parallel configuration. The spectra were acquired at 12 K and using 488 nm excitation wavelength. Both configurations were measured under the same experimental conditions. For legibility the spectra are shifted vertically by a constant value. Raman peaks at 148, 224, 287 and 341 cm^{-1} are highlighted as representative peaks with characteristic polarization intensity behavior.

peaks centered at 95 cm^{-1} and 224 cm^{-1} exhibit a constant intensity in parallel configuration and cancelled in perpendicular configuration (Fig. 4(b)). This is a typical behavior of A_{1g} modes, as pointed out in Table 1. In contrast, the intensity of Raman peaks at 109 cm^{-1}, 148 cm^{-1}, 201 cm^{-1}, and 309 cm^{-1} evolve sinusoidally in both configurations, as shown in Fig. 4(c). This is consistent with the behavior of B_{1g} modes.

Interestingly, some angular dependencies of peak intensities show a significant intensity offset between the parallel and perpendicular configurations in addition to their sinusoidal evolution. This is the case of the Raman peak at 341 cm^{-1}, as shown in Fig. 4(d). This attests an A_{1g} mode superimposed to the present B_{1g} or B_{2g} modes. Hence the peaks observed at 87 cm^{-1}, 330 cm^{-1}, and 341 cm^{-1} are resulting from A_{1g} and B_{1g} contributions, while the peak at 210 cm^{-1} arises from a superposition of the A_{1g} and a B_{2g} phonon modes.

Finally, the peak around 287 cm^{-1} has the most complex intensity behavior. Observed variation in this peak position with polarization angles (Fig. S1 in the ESI†), as well as wider peak width when compared to other peaks in the Raman spectra, indicate superposition of two or more vibrational modes in this region. Perpendicular configuration offers easer resolution of this peak, considering that the A_{1g} modes are cancelled in this case. Based on the overall intensity dependence with the polarization angle for this peak, it is reasonable to assume that it consists of one B_{1g} and one B_{2g} mode. Having in mind the phase opposition in the intensity behavior between B_{1g} and B_{2g} modes for different polarization angles, these two phonons cannot be simultaneously cancelled or fully activated. This means that for certain polarization angles θ only B_{1g} mode will be activated, while B_{2g} mode will be canceled. On the other hand, the situation is reversed for polarization angle $\theta + \pi/4$, where B_{2g} mode is activated, while B_{1g} is canceled. Raman spectra measured under such polarization conditions are presented in Fig. S2(a) in the ESI.† Deconvolution of the Raman spectra measured under these conditions, with Lorentzian curves, has allowed the exact determination of the positions for the weak B_{2g} mode centered at 287 cm^{-1} and the B_{1g} mode centered at 290 cm^{-1}. Fig. S2(b) in the ESI† presents an example of the deconvolution under polarization angles for which both B_{1g} or B_{2g} mode are activated. Fig. 4(e) shows the angle resolved intensity dependence of the B_{1g} and B_{2g} modes obtained from the 287 cm^{-1} peak deconvolution for each polarization angle in perpendicular configuration. This observed intensity dependence agrees well with the expected behavior for both B_{1g} and B_{2g} modes as presented in Table 1.

The above-mentioned methodology has been applied to all measured Raman spectra and has allowed identification of positions and the angle resolved intensity profiles of 17 Raman active modes in the case of the monocrystalline Zn_3P_2 with (001) growth orientation perpendicular to the substrate (Fig. 3). The positions of these modes and their symmetry assignment are listed in Fig. 5, along with the comparison to ref. 23 and 35. Most of the observed Raman peaks are perfectly consistent with those reported in ref. 35. However, two peaks behave unexpectedly. The peak at 103 cm^{-1} has a periodic intensity dependence from polarization angle in both parallel and perpendicular configuration which does not correspond to either B_{1g} or B_{2g} mode (Fig. S3 in the ESI†). This is in contrast to DFT calculations which predict a B_{1g} mode at this position. Furthermore, the intensity evolution of the peak at 109 cm^{-1} suggests an assignment to B_{1g} mode (Fig. S4 in the ESI†), in contrast to an E_g mode reported at this position in ref. 35. Considering that the two peak frequencies are close, it is most likely that the Raman peak at 109 cm^{-1} should be assigned to the B_{1g} mode, while the peak at 103 cm^{-1} may in fact correspond to an activated E_g mode or a multi-phonon contribution. Considering that the width of the peak at 103 cm^{-1} is similar to the widths of the other peaks in the Raman spectra belonging to one-phonon modes, it is most likely that the multi-phonon contribution could be discarded. Even though E_g modes are silent under the used polarization configurations, geometrical reasons can lead to their

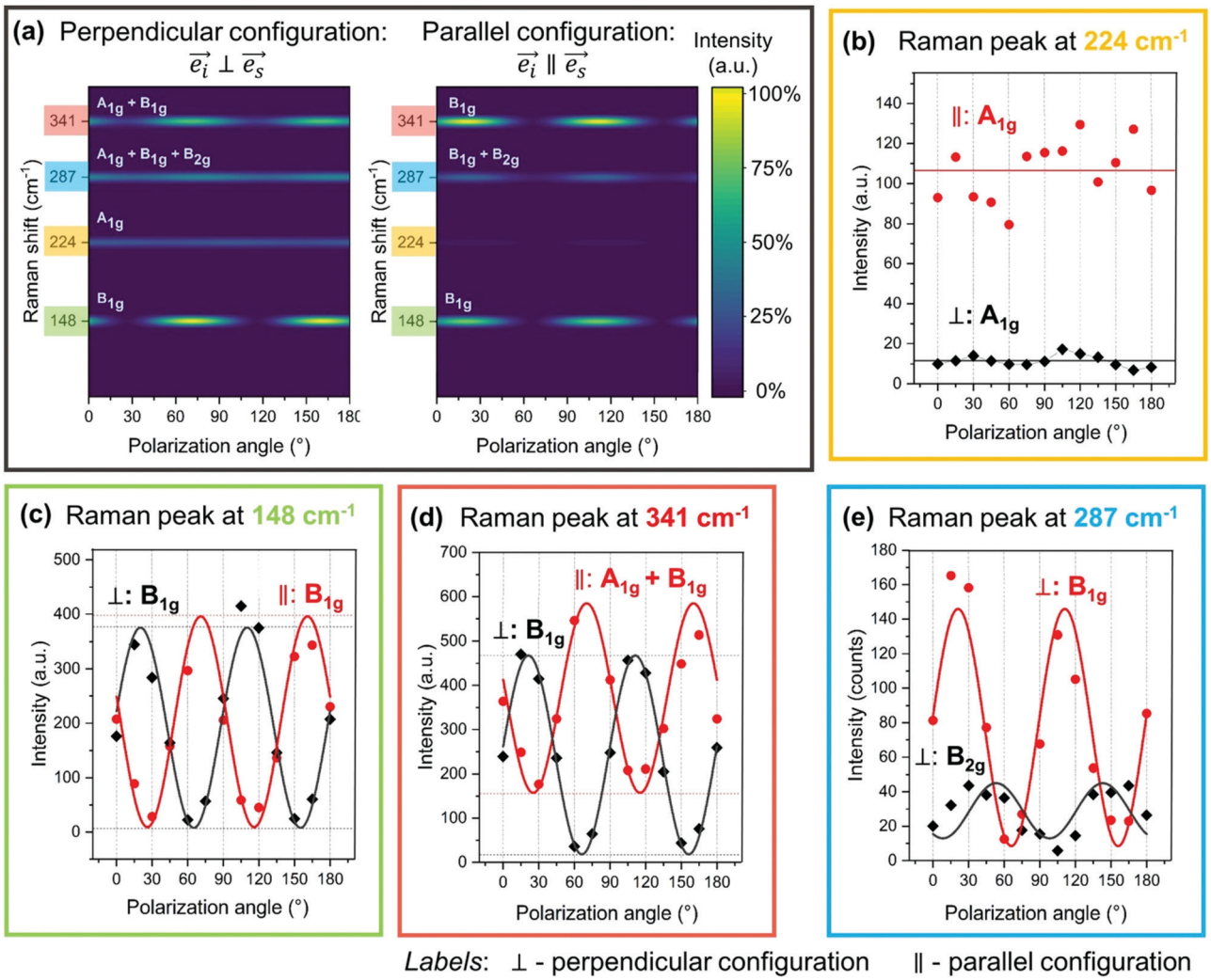

Fig. 4 (a) Calculated Raman intensity profiles in dependence of polarization angle in perpendicular and parallel configurations for four representative Raman peaks. (b–e) Polarization-dependent Raman intensities for four characteristic Raman peaks centered at 224, 148, 341 and 287 cm^{-1}, showing the modeling of the experimental data according to the equations presented in Table 1 and allowing calculation of the Raman tensor elements. Dot and diamond symbols represent the experimental data, while full lines present the fits. The standard uncertainty in the intensity (represented by dots and diamonds in the figure) is considered to be ±5%.

accidental activation,[43] such as a slightly titled sample or outer rays from the microscope that result in a vertical component of the incident polarization vector. This same reason may explain the unexpected weak Raman contribution at 320 cm^{-1}, corresponding to an activated E_g mode, as reported in ref. 35, with a similar intensity evolution as the peak at 103 cm^{-1} (Fig. S5 in the ESI†).

3.4 Raman tensor coefficients

Raman tensor elements were calculated for each mode based on the fittings of the Raman intensity dependence with the polarization angle by using equations presented in Table 1. Representative examples of fittings are presented in Fig. 4(b–e). The obtained coefficients are summarized in Table 2. Coefficients *c* have been calculated twice from both perpendicular and parallel polarization configurations and show to be in good agreement. All Raman tensor elements are normalized to the coefficient of the B_{1g} mode at 309 cm^{-1} in perpendicular configuration. It should be noted that Raman tensor element *b* corresponding to the A_{1g} mode and element *e* corresponding to the E_g modes could not be calculated in this case, due to the selection rules which apply for the Raman excitation on the (001)-plane basal plane of Zn_3P_2.

The uncertainties on the tensor elements were estimated using the student's *t*-distribution based on the fitting standard deviation, assuming that the experimental points are normally distributed around the theoretical curve.[44] The uncertainty generated by the peak centering, that feeds through the tensor elements because of the $C(\omega_p)$ factor, is negligible and thus not considered. The reflection-induced ellipticity is negligible in our setup, and the spectrum baseline has been subtracted individually following the photoluminescence spectrum line shape, thus avoiding interferences with the baseline angular dependency.

3.5 Raman spectra simulations of Zn_3P_2 and comparison with the experiments

Raman tensor element calculations for Zn_3P_2 were performed in order to compare them with the experimental values. The values

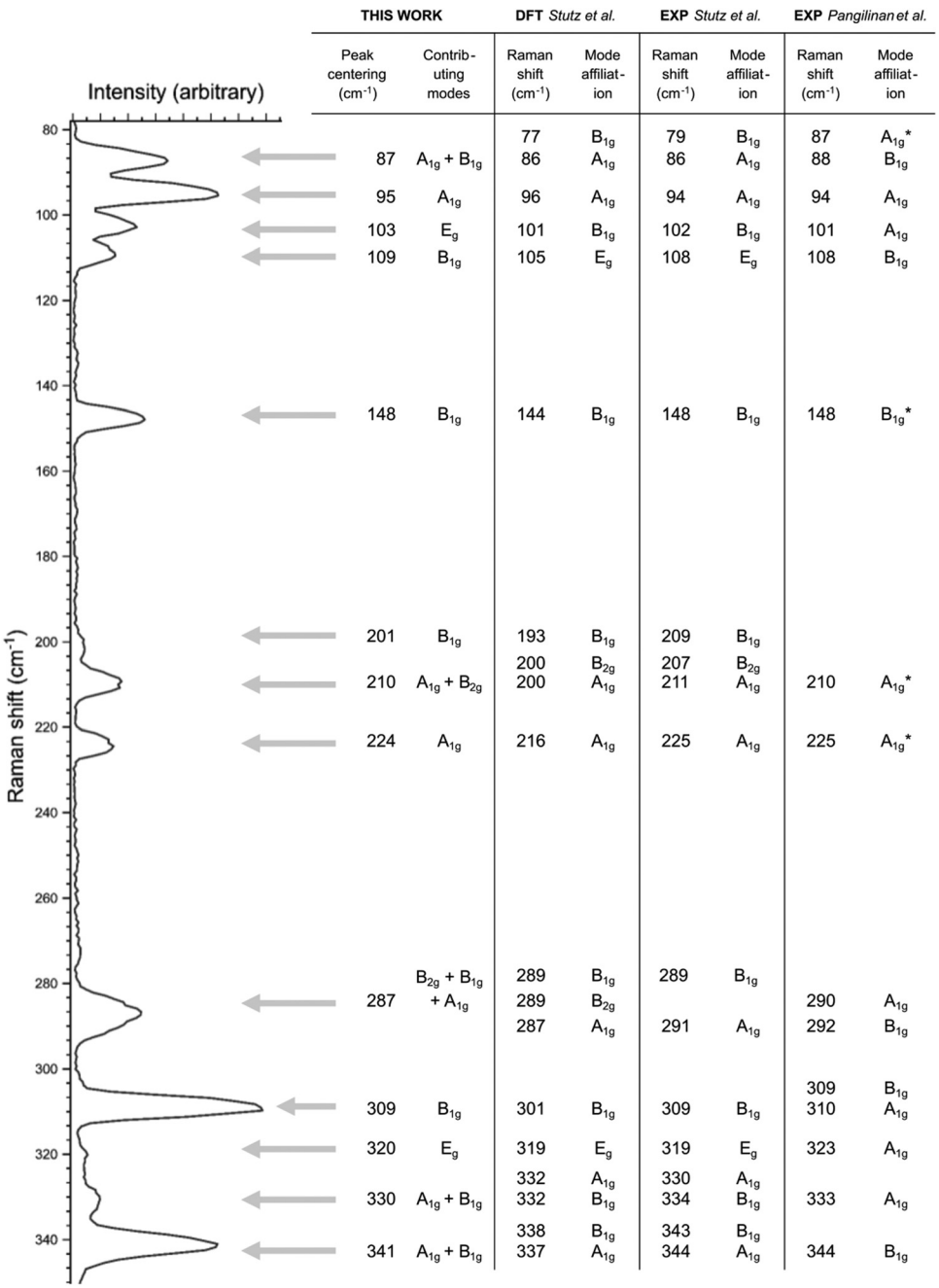

THIS WORK		DFT *Stutz et al.*		EXP *Stutz et al.*		EXP *Pangilinan et al.*	
Peak centering (cm^{-1})	Contributing modes	Raman shift (cm^{-1})	Mode affiliation	Raman shift (cm^{-1})	Mode affiliation	Raman shift (cm^{-1})	Mode affiliation
		77	B_{1g}	79	B_{1g}	87	A_{1g}*
87	$A_{1g} + B_{1g}$	86	A_{1g}	86	A_{1g}	88	B_{1g}
95	A_{1g}	96	A_{1g}	94	A_{1g}	94	A_{1g}
103	E_g	101	B_{1g}	102	B_{1g}	101	A_{1g}
109	B_{1g}	105	E_g	108	E_g	108	B_{1g}
148	B_{1g}	144	B_{1g}	148	B_{1g}	148	B_{1g}*
201	B_{1g}	193	B_{1g}	209	B_{1g}		
		200	B_{2g}	207	B_{2g}		
210	$A_{1g} + B_{2g}$	200	A_{1g}	211	A_{1g}	210	A_{1g}*
224	A_{1g}	216	A_{1g}	225	A_{1g}	225	A_{1g}*
	$B_{2g} + B_{1g}$	289	B_{1g}	289	B_{1g}		
287	$+ A_{1g}$	289	B_{2g}			290	A_{1g}
		287	A_{1g}	291	A_{1g}	292	B_{1g}
						309	B_{1g}
309	B_{1g}	301	B_{1g}	309	B_{1g}	310	A_{1g}
320	E_g	319	E_g	319	E_g	323	A_{1g}
		332	A_{1g}	330	A_{1g}		
330	$A_{1g} + B_{1g}$	332	B_{1g}	334	B_{1g}	333	A_{1g}
		338	B_{1g}	343	B_{1g}		
341	$A_{1g} + B_{1g}$	337	A_{1g}	344	A_{1g}	344	B_{1g}

Fig. 5 Raman spectrum of monocrystalline Zn_3P_2 thin film measured in parallel configuration $(\vec{e_i} \parallel \vec{e_S})$ for polarization angle of $\theta = 22.5^\circ$, allowing activation of B_{1g}, B_{2g} and A_{1g} modes. Each Raman peak is identified with a position and symmetry assignment as indicated in the table under "This work" column. These are compared with previously reported data based on DFT simulations (column "DFT Stutz *et al.*"[35]) and experiments (columns "EXP Stutz *et al.*"[35] and "EXP Pangilinan *et al.*"[23]). Asterix symbol (*) in the column "EXP Pangilinan *et al.*" denotes an affiliation to acceptor defect states identified in ref. 23.

were calculated from the first-order dielectric tensor for the equilibrium crystal configuration and for the crystal with atomic displacement according to the vibrational patterns of the individual phonon modes. Raman intensities were then calculated according to equations given in Table 1 and using theoretical values of the Raman tensor elements coupled with the experimental conditions (polarization configuration, laser wavelength and temperature) in agreement with our Raman measurements.

Fig. 6 presents the comparison between the calculated intensities of the Raman modes and the experimental Raman spectra for four polarization configurations, including parallel $(\vec{e_i} \parallel \vec{e_S})$ and perpendicular $(\vec{e_i} \perp \vec{e_S})$ geometries with various polarization angles (θ). These configurations allow activation of different types of phonon modes, such as B_{1g}, B_{2g} and A_{1g} in case of Fig. 6(a and b), B_{1g} and A_{1g} in case of Fig. 6(c) and B_{1g} in case of Fig. 6(d). The variety of polarization configurations

Table 2 Raman tensor coefficients obtained from the fit parameters of the angular intensity dependencies of the phonon modes for Zn_3P_2. All elements are normalized to the Raman tensor coefficient of the B_{1g} mode at 309 cm^{-1} in perpendicular configuration. Labels: ν_R (cm^{-1}) – Raman mode frequency; $\parallel$ – parallel polarization configuration; $\perp$ – perpendicular polarization configuration

A_{1g} modes		B_{1g} modes			B_{2g} modes	
ν_R (cm^{-1})	Coefficient a	ν_R (cm^{-1})	Coefficient c ($\parallel$)	Coefficient c ($\perp$)	ν_R (cm^{-1})	Coefficient d
86	7.1 ± 0.9	79	4.9 ± 1.7	3.8 ± 0.6	207	2.5 ± 0.7
95	8.5 ± 1.1	109	5.4 ± 0.6	6.7 ± 1.0	287	1.5 ± 0.6
210	3.2 ± 0.4	148	9.2 ± 1.1	9.0 ± 0.6		
224	3.7 ± 0.6	201	2.4 ± 0.3	2.6 ± 0.2		
287	3.3 ± 0.6	290		3.9 ± 0.4		
330	2.0 ± 0.5	309	9.6 ± 1.2	10.0 ± 0.4		
343	3.6 ± 1.2	334	2.0 ± 0.5	2.3 ± 0.3		
		341	6.3 ± 0.9	6.4 ± 0.2		

serves as reliable way for comparison between the experimental and theoretical results.

Overall, Fig. 6 suggests a very good agreement between the theory and experiment. In particular, calculated intensities of the B_{1g} and B_{2g} modes match very well the measured Raman spectra in the high frequency region (>150 cm^{-1}). In contrast, there is slightly more discrepancy between the experimental and calculated values in Raman intensities of these modes in the lower frequency region (<150 cm^{-1}). Additionally, it is noticed that calculated intensities of the A_{1g} modes are usually over estimated in the high frequency region, and under estimated in the low frequency region. There are several possible reasons for these kinds of discrepancies. First reason is related to the way Raman intensities are calculated in DFT, where certain approximations are necessary for making feasible calculations. These include approximations in the many body interactions, which can become especially important for structures with large number of atoms, such as Zn_3P_2. Other possible sources of mismatch in the simulations include the use of a structure optimized at 0 K, as well as a periodic crystal with no treatment of defects or disorder. Defects especially can affect the intensities of Raman modes.[30,31] Considering that Zn_3P_2 is intrinsically p-type semiconductor, due to the low energy formation of P interstitials,[26] it is possible that these intrinsic defects are

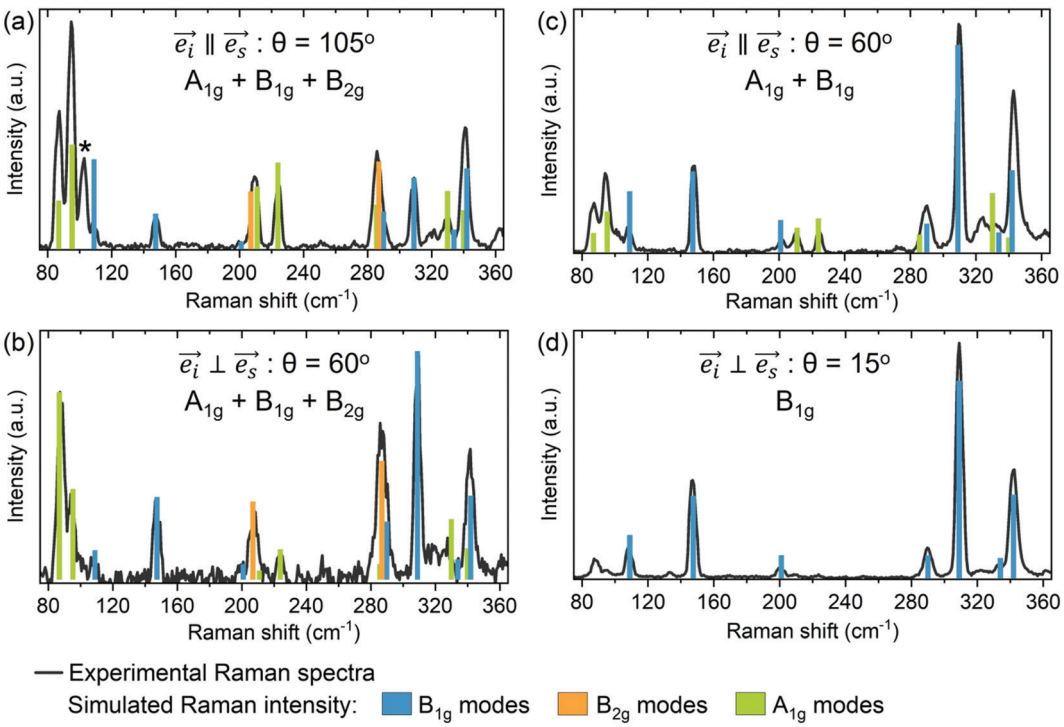

Fig. 6 Comparison between the calculated intensity of the Raman modes (colored bars) and the experimental Raman spectra (black line) for four different polarization configurations allowing activation of different phonon modes: (a) parallel configuration ($\vec{e_i} \parallel \vec{e_S}$) with polarization angle of $\theta = 105°$, allowing activation of B_{1g}, B_{2g} and A_{1g} modes; (b) perpendicular configuration ($\vec{e_i} \perp \vec{e_S}$) with polarization angle of $\theta = 60°$, allowing activation of B_{1g}, B_{2g} and A_{1g} modes; (c) parallel configuration ($\vec{e_i} \parallel \vec{e_S}$) with polarization angle of $\theta = 60°$, allowing activation of B_{1g} and A_{1g} modes; and (d) perpendicular configuration ($\vec{e_i} \perp \vec{e_S}$) with polarization angle of $\theta = 15°$, allowing activation of B_{1g} modes. Asterix symbol (*) denotes the position of the activated E_g mode.

affecting the intensities of certain modes in the Raman spectra, and thus creating discrepancy between the experimental and theoretical results. Pangilinan *et al.* has suggested several A_{1g} and B_{1g} modes which could be related to acceptor states in the Raman spectrum of Zn_3P_2.[23] Considering that literature reports on defects structure in Zn_3P_2 are limited, further experimental and theoretical explorations on Zn_3P_2 defect states are planned in the future for better optimization of the material for optoelectronic applications.

Conclusion

Vibrational properties of stoichiometric monocrystalline Zn_3P_2 were reported from angle-resolved polarization Raman measurements and first-principles calculations. Particular focus was put on the intensity evolution of the Raman modes under different polarization configurations. This has allowed determination of the Raman tensor elements characteristic for A_{1g}, B_{1g} and B_{2g} vibrational modes. Simulation of the Raman peak intensities from first-principles calculations allowed direct comparison between the experimental and theoretical values of the Raman tensor elements. Overall good agreement is found between the experimental and simulated Raman spectra of Zn_3P_2 for various polarization configurations, providing a platform for future investigations concerning defects in this material.

Conflicts of interest

The authors declare that they have no competing financial interests.

Acknowledgements

The authors gratefully acknowledge support from the Swiss National Science Foundation (SNSF) through project BSCGI0_157705 and by the Max Planck-EPFL Center for Molecular Nanoscience and Technology. M. D. thanks funding from H2020 through the Marie Curie Project SMARTCELL (project number 101022257).

References

1 L. Bryja, K. Jezierski and J. Misiewicz, Optical properties of Zn_3P_2 thin films, *Thin Solid Films*, 1993, **229**, 11–13.
2 J. Misiewicz, L. Bryja, K. Jezierski, J. Szatkowski, N. Mirowska, Z. Gumienny and E. Placzek-Popko, Zn_3P_2 – A new material for optoelectronic devices, *Microelectron. J.*, 1994, **25**, xxiii–xxviii.
3 N. C. Wyeth and A. Catalano, Spectral response measurements of minority-carrier diffusion length in Zn_3P_2, *J. Appl. Phys.*, 1979, **50**, 1403–1407.
4 G. M. Kimball, A. M. Müller, N. S. Lewis and H. A. Atwater, Photoluminescence-based measurements of the energy gap and diffusion length of Zn_3P_2, *Appl. Phys. Lett.*, 2009, **95**, 112103.
5 B. A. Glassy and B. M. Cossairt, II_3V_2 (II: Zn, Cd; V: P, As) semiconductors: From bulk solids to colloidal nanocrystals, *Small*, 2017, **13**, 1702038.
6 B. A. Glassy and B. M. Cossairt, Ternary synthesis of colloidal Zn_3P_2 quantum dots, *Chem. Commun.*, 2015, **51**, 5283–5286.
7 C. Wadia, A. P. Alivisatos and D. M. Kammen, Materials availability expands the opportunity for large-scale photovoltaics deployment, *Environ. Sci. Technol.*, 2009, **43**, 2072–2077.
8 V. S. Vavilov, V. D. Negrei, I. V. Potykevich, Y. V. Potykevich, A. V. Fedotovskii and M. V. Chukichev, Radiative recombination of zinc diphosphide, *Phys. Status Solidi B*, 1972, **49**, K103–K106.
9 V. V. Sobolev and A. I. Kozlov, Free exciton and exciton-impurity complexes of zinc diphosphide and zinc diarsenide, *Phys. Status Solidi B*, 1984, **126**, K59–K62.
10 N. C. Wyeth and A. Catalano, Barrier heights of evaporated metal contacts on Zn_3P_2, *J. Appl. Phys.*, 1980, **51**, 2286–2288.
11 P. S. Nayar and A. Catalano, Zinc phosphide-zinc oxide heterojunction solar cells, *Appl. Phys. Lett.*, 1981, **39**, 105–107.
12 A. Catalano and M. Bhushan, Evidence of p/n homojunction formation in Zn_3P_2, *Appl. Phys. Lett.*, 1980, **37**, 567–569.
13 M. Bhushan and A. Catalano, Polycrystalline Zn_3P_2 Schottky barrier solar cells, *Appl. Phys. Lett.*, 1981, **38**, 39–41.
14 M. Dimitrievska, F. S. Hage, S. E. Steinvall, A. P. Litvinchuk, E. Z. Stutz, Q. M. Ramasse and A. F. I. Morral, The advantage of nanowire configuration in band structure determination, *Adv. Funct. Mater.*, 2021, 2105426.
15 S. Escobar Steinvall, N. Tappy, M. Ghasemi, R. R. Zamani, T. LaGrange, E. Z. Stutz, J.-B. Leran, M. Zamani, R. Paul and A. Fontcuberta i Morral, Multiple morphologies and functionality of nanowires made from earth-abundant zinc phosphide, *Nanoscale Horiz.*, 2020, **5**, 274–282.
16 G. Z. Shen, Y. Bando, J. Q. Hu and D. Golberg, Single-crystalline trumpetlike zinc phosphide nanostructures, *Appl. Phys. Lett.*, 2006, **88**, 143105.
17 R. Yang, Y.-L. Chueh, J. R. Morber, R. Snyder, L.-J. Chou and Z. L. Wang, Single-crystalline branched zinc phosphide nanostructures: Synthesis, properties, and optoelectronic devices, *Nano Lett.*, 2007, **7**, 269–275.
18 E. J. Luber, M. H. Mobarok and J. M. Buriak, Solution-processed zinc phosphide (α-Zn_3P_2) colloidal semiconducting nanocrystals for thin film photovoltaic applications, *ACS Nano*, 2013, **7**, 8136–8146.
19 M. Zamani, E. Stutz, S. Escobar, R. R. Zamani, R. Paul, J.-B. Leran, M. Dimitrievska and A. Fontcuberta i Morral, The path towards 1 μm monocrystalline Zn_3P_2 films on InP: Substrate preparation, growth conditions and luminescence properties, *J. Phys.: Energy*, 2021, **3**, 034011.
20 S. Escobar Steinvall, E. Z. Stutz, R. Paul, M. Zamani, N. Y. Dzade, V. Piazza, M. Friedl, V. de Mestral, J.-B. Leran, R. R. Zamani and A. Fontcuberta i Morral, Towards defect-free thin films of the earth-abundant absorber zinc phosphide by nanopatterning, *Nanoscale Adv.*, 2021, **3**, 326–332.
21 R. Paul, N. Humblot, S. E. Steinvall, E. Z. Stutz, S. S. Joglekar, J.-B. Leran, M. Zamani, C. Cayron, R. Logé,

A. G. del Aguila, Q. Xiong and A. F. I. Morral, van der Waals epitaxy of earth-abundant Zn_3P_2 on graphene for photovoltaics, *Cryst. Growth Des.*, 2020, **20**, 3816–3825.

22 J. Misiewicz, Optical vibrations in the Zn_3P_2 lattice, *J. Phys.: Condens. Matter*, 1989, **1**, 9283–9299.

23 G. Pangilinan, R. Sooryakumar and J. Misiewicz, Raman activity of Zn_3P_2, *Phys. Rev. B: Condens. Matter Mater. Phys.*, 1991, **44**, 2582–2588.

24 A. Catalano and R. B. Hall, Defect dominated conductivity in Zn_3P_2, *J. Phys. Chem. Solids*, 1980, **41**, 635–640.

25 S. Demers and A. van de Walle, Intrinsic defects and dopability of zinc phosphide, *Phys. Rev. B: Condens. Matter Mater. Phys.*, 2012, **85**, 195208.

26 W.-J. Yin and Y. Yan, The electronic properties of point defects in earth-abundant photovoltaic material Zn_3P_2: A hybrid functional method study, *J. Appl. Phys.*, 2013, **113**, 013708.

27 M. Dimitrievska, F. Boero, A. P. Litvinchuk, S. Delsante, G. Borzone, A. Perez-Rodriguez and V. Izquierdo-Roca, Structural polymorphism in ''Kesterite'' Cu_2ZnSnS_4: Raman spectroscopy and first-principles calculations analysis, *Inorg. Chem.*, 2017, **56**, 3467–3474.

28 T. Sander, C. T. Reindl, M. Giar, B. Eifert, M. Heinemann, C. Heiliger and P. J. Klar, Correlation of intrinsic point defects and the Raman modes of cuprous oxide, *Phys. Rev. B: Condens. Matter Mater. Phys.*, 2014, **90**, 045203.

29 M. Bruna, A. K. Ott, M. Ijäs, D. Yoon, U. Sassi and A. C. Ferrari, Doping dependence of the Raman spectrum of defected graphene, *ACS Nano*, 2014, **8**, 7432–7441.

30 M. Dimitrievska, F. Oliva, M. Guc, S. Giraldo, E. Saucedo, A. Pérez-Rodríguez and V. Izquierdo-Roca, Defect characterisation in $Cu_2ZnSnSe_4$ kesterites *via* resonance Raman spectroscopy and the impact on optoelectronic solar cell properties, *J. Mater. Chem. A*, 2019, **7**, 13293–13304.

31 M. Dimitrievska, A. Fairbrother, E. Saucedo, A. Pérez-Rodríguez and V. Izquierdo-Roca, Influence of compositionally induced defects on the vibrational properties of device grade $Cu_2ZnSnSe_4$ absorbers for kesterite based solar cells, *Appl. Phys. Lett.*, 2015, **106**, 073903.

32 M. Dimitrievska, A. Fairbrother, E. Saucedo, A. Pérez-Rodríguez and V. Izquierdo-Roca, Secondary phase and Cu substitutional defect dynamics in kesterite solar cells: Impact on optoelectronic properties, *Sol. Energy Mater. Sol. Cells*, 2016, **149**, 304–309.

33 M. Dimitrievska, A. Fairbrother, A. Pérez-Rodríguez, E. Saucedo and V. Izquierdo-Roca, Raman scattering crystalline assessment of polycrystalline Cu_2ZnSnS_4 thin films for sustainable photovoltaic technologies: Phonon confinement model, *Acta Mater.*, 2014, **70**, 272–280.

34 A. Hashemi, A. V. Krasheninnikov, M. Puska and H.-P. Komsa, Efficient method for calculating Raman spectra of solids with impurities and alloys and its application to two-dimensional transition metal dichalcogenides, *Phys. Rev. Mater.*, 2019, **3**, 023806.

35 E. Z. Stutz, S. Escobar Steinvall, A. P. Litvinchuk, J.-B. Leran, M. Zamani, R. Paul, A. Fontcuberta i Morral and M. Dimitrievska, Raman spectroscopy and lattice dynamics calculations of tetragonally-structured single crystal zinc phosphide (Zn_3P_2) nanowires, *Nanotechnology*, 2021, **32**, 085704.

36 A. Eckmann, A. Felten, A. Mishchenko, L. Britnell, R. Krupke, K. S. Novoselov and C. Casiraghi, Probing the nature of defects in graphene by Raman spectroscopy, *Nano Lett.*, 2012, **12**, 3925–3930.

37 D. M. Ceperley and B. J. Alder, Ground state of the electron gas by a stochastic method, *Phys. Rev. Lett.*, 1980, **45**, 566–569.

38 J. P. Perdew and A. Zunger, Self-interaction correction to density-functional approximations for many-electron systems, *Phys. Rev. B: Condens. Matter Mater. Phys.*, 1981, **23**, 5048–5079.

39 S. J. Clark, M. D. Segall, C. J. Pickard, P. J. Hasnip, M. I. J. Probert, K. Refson and M. C. Payne, First principles methods using CASTEP, *Z. Kristallogr. – Crystall. Mater.*, 2005, **220**, 567–570.

40 I. E. Zanin, K. B. Aleinikova, M. M. Afanasiev and M. Y. Antipin, *J. Struct. Chem.*, 2004, 844–848.

41 S. V. Gallego, J. Etxebarria, L. Elcoro, E. S. Tasci and J. M. Perez-Mato, Automatic calculation of symmetry-adapted tensors in magnetic and non-magnetic materials: A new tool of the Bilbao Crystallographic Server, *Acta Crystallogr., Sect. A: Found. Adv.*, 2019, **75**, 438–447.

42 W. (William) Hayes, *Scattering of light by crystals/William Hayes, Rodney Loudon*, Wiley, New York, 1978.

43 T. Sander, S. Eisermann, B. K. Meyer and P. J. Klar, Raman tensor elements of wurtzite ZnO, *Phys. Rev. B: Condens. Matter Mater. Phys.*, 2012, **85**, 165208.

44 R. J. Beckman and M. E. Johnson, Fitting the student-t distribution to grouped data, with application to a particle scattering experiment, *Technometrics*, 1987, **29**, 17–22.

